Non-Hermitian nanophotonic and plasmonic waveguides

Hadiseh Alaeian[1,2] and Jennifer A. Dionne[2]

[1]*Department of Electrical Engineering, Stanford University, Stanford, California 94305, USA*

[2]*Department of Materials Science and Engineering, Stanford University, Stanford, California 94305, USA*

(Received 23 December 2013; revised manuscript received 29 January 2014; published 27 February 2014)

Non-Hermitian Hamiltonians arising from parity-time (PT)-symmetric potentials have been extensively explored in optical systems, owing to their ability to generate asymmetric and even nonreciprocal light propagation. In this paper, we investigate such PT potentials in plasmonic systems, demonstrating asymmetric optical propagation in deeply subwavelength waveguides. In particular, we investigate a five layer plasmonic waveguide composed of metallic layers separated by dielectric media containing either loss or gain in equal quantities. Through an analytic solution of Maxwell's equations, we identify the four lowest order modes of the waveguide, including two positive index modes and two negative index modes, and investigate their evolution with increasing but balanced gain and loss, κ. Both the exact analytic approach and an approximate one based on Rayleigh-Schrodinger perturbation theory demonstrate eigenvalue merging and state coalescence with increasing κ, unlike the familiar energy-level splitting observed in conventional coupled systems. The state coalescence always occurs between modes of opposite parity. Also, by changing the coupling between the waveguide layers, state coalescence can occur between modes with opposite refractive indices, resulting in the merging of a positive index mode with a negative index mode at the exceptional point. We use dispersion diagrams and field profiles to illustrate the asymmetric plasmon propagation properties with increasing κ. We also show that at the system's exceptional point, the modal power varies quadratically along the waveguide. This study represents a spectral analysis of deeply subwavelength PT-symmetric plasmonic and multimodal photonic waveguides and provides a foundation for designing asymmetric and unidirectional nanophotonic devices.

DOI: 10.1103/PhysRevB.89.075136 PACS number(s): 73.20.Mf, 73.40.Rw, 42.82.Et

I. INTRODUCTION

In the past decade, plasmonic components such as lasers [1–5], spasers [6–9], modulators [10–14], waveguides [15–21], and detectors have provided a route toward optical communication and computation on deeply subwavelength scales. As these components rely on plasmons—collective oscillations of conduction electrons in a metal coupled to photons in a dielectric—their spatial footprint is much smaller than conventional optical devices. Additionally, because plasmons are characterized by very strong electromagnetic field intensities, these components exhibit enhanced nonlinearities compared to conventional optical components. For example, plasmonic lasers can now exhibit thresholdless behavior [5], even at room temperature, and plasmonic modulators have been demonstrated with input powers as low as femtowatts and bandwidths exceeding 100 THz [22,23].

Despite this progress, electronic devices still exhibit one key advantage over plasmonic and photonic components: They rely on charged carriers (electrons), which, with appropriate electronic potentials, can exhibit nonreciprocal signal propagation. Such nonreciprocity is critical to construct devices such as diodes and circulators. While recent research efforts have utilized static magnetic fields and paramagnetic materials to break the reciprocity of optical or plasmonic signal propagation [24–27], these strategies rely on somewhat bulky elements, and so may not be ideally suited for on-chip nanophotonics. An alternate strategy to achieve asymmetric and directional optical propagation relies on non-Hermitian, parity-time (PT)-symmetric optical potentials.

PT-symmetric potentials first arose in the context of quantum mechanics. Bender and colleagues demonstrated that Hermiticity is a sufficient but not necessary condition to ensure real-valued eigenvalues [28–31]. Instead, the weaker condition of PT symmetry ensures a real spectrum below a certain threshold. Above this threshold, the eigenvalues of the system cease to be real and become complex conjugates of each other. In relating this concept to optics, researchers have noted that the paraxial wave equation and Schrodinger equation are isomorphic, with time evolution substituted with wave propagation. In this case, the refractive index of the structure takes on the role of the potential in quantum mechanics. The required condition of the system potential to be PT symmetric is translated to the permittivity properties as $\epsilon(r) = \epsilon^*(-r)$. In other words, to achieve a PT-symmetric optical potential, the real part of the permittivity must be an even function of position while its imaginary part must be odd.

To date, PT-symmetric potentials in optics have been used to attain nonreciprocal reflection, unidirectional invisibility [32–34], power oscillations, and electromagnetic induced transparency (EIT). Double refraction, band merging, asymmetric power transmission, and transitions from lasing to perfect absorption have also been observed [35–40]. Further, the inclusion of nonlinear materials in PT systems has been suggested as a platform to excite optical solitons [41–43] and to realize optical insulators and diodes [44].

In this paper, building on the extensive foundation of PT-symmetric optics, we investigate the modal properties of PT-symmetric plasmonic waveguides. In particular, we focus on a five-layer planar metal-insulator (MIMIM) structure—perhaps the simplest yet most fundamental PT-symmetric plasmonic waveguide. As seen in Fig. 1, it is composed of metallic layers separated by dielectric media containing either loss or gain in equal quantities. Our study is unique in that, unlike most wavelength-scale PT-optical studies, we do not rely on a paraxial wave approximation or coupled

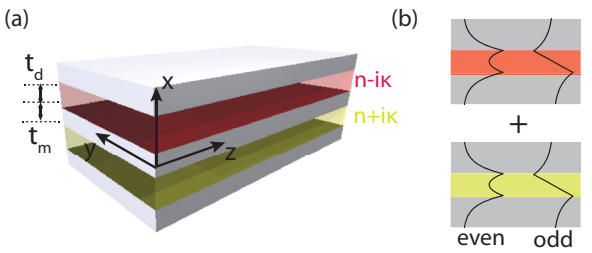

FIG. 1. (Color online) (a) Schematic of the five-layer plasmonic waveguide, composed of planar metallic slabs separated by loss (yellow, $n + i\kappa$) or gain (red, $n - i\kappa$) media. The waveguide can be considered as a system of two coupled three-layer MIM waveguides as shown in (b). For a sufficiently thin dielectric, each MIM waveguide supports only two modes with even and odd symmetries. The typical magnetic field profile of these even and odd modes is shown by the black curves in each waveguide.

mode theory, which would both fail in this regime. Rather, we use exact solutions of Maxwell's equations to investigate the dispersion, propagation, field distribution, and power evolution as a function of the loss/gain parameter.

Our paper is organized as follows: In the first section, we determine the transverse-magnetic (TM) modes of a five-layer PT-symmetric MIMIM plasmonic waveguide. Our calculations illustrate eigenmode evolution and the crossing of the mode propagation constants with increasing non-Hermiticity parameter. Then, we demonstrate how tuning the coupling between the metallic and dielectric layers of the MIMIM waveguide affects state coalescence and propagation constant merging. In the second section, we develop a Hamiltonian formulation of electromagnetic wave propagation in the waveguide. This formulation allows us to derive the perturbational solution for the mode propagation constants with increasing loss/gain, providing key insight into the physics of mode merging and coalescence. This Hamiltonian formulation also allows us to study the modal properties right at the exceptional point, revealing the existence of two independent solutions. One solution has the form of a typical waveguide mode, with a real propagation constant and a constant power along the direction of propagation, while the second solution has the same propagation constant but a power that varies quadratically along the waveguide. These results motivate the introduction of a conserved quantity in PT-symmetric waveguides, the generalized power. In the final section, we discuss likely applications for PT-symmetric plasmonic waveguides, including low-power and fast optical modulators with gain and nonlinear, nonrecripocal optical components. We note that while our discussion focuses on waveguide geometries, our derivation and results can be extended to other coupled PT-symmetric systems, such as coupled resonators and quantum wells.

II. EXACT MODAL SOLUTION TO PLASMON PROPAGATION IN PT-SYMMETRIC POTENTIALS

A. PT-symmetric plasmon dispersion

Figure 1(a) illustrates the five-layer plasmonic waveguide studied in this paper. We consider silver as the metallic layer, with a permittivity described by a lossless Drude model: $\epsilon_{Ag} = 1 - (\frac{\omega_p}{\omega})^2$, with ω_p (the bulk plasma frequency of silver) equal to $8.85 \times 10^{15} \frac{\text{rad}}{\text{sec}}$ [45]. We consider a lossless Drude model to highlight the emergent features of PT potentials in plasmonic waveguide systems, but note that similar effects are obtained with a lossy metal (see, i.e. Ref. [46]). The dielectric layers are assumed to be TiO_2 with real(ϵ_{TiO_2}) = 10.2 [real(n) = 3.2]. Parameter κ corresponds to the amount of loss or gain in the dielectric layers, and is hereafter called the *non-Hermiticity* parameter. Note that regardless of the value of κ, loss and gain are always balanced in the system. As seen in Fig. 1(b), our system can be viewed as two MIM plasmonic waveguides, each supporting a symmetric and antisymmetric plasmon mode, coupled through the metallic layer. The transverse-magnetic (TM) modes of this five-layer MIMIM system are described by

$$\left(\frac{d^2}{dx^2} + k_0^2\epsilon_l - k_z^2\right) H_{y_l}(x) = 0, \tag{1}$$

where k_z is the wave vector along the propagation direction z, $H_{yl}(x)$ is the magnetic field, and the subscript l denotes the lth layer.

Using the transfer matrix formalism described in Ref. [17], we obtain the dispersion relations. First, we consider metallic and dielectric layer thicknesses of $t_m = t_d = 30$ nm. Figure 2(a) shows the dispersion curves of the four lowest order modes, labeled B_1, B_2, B_3, and B_4, of the structure as a function of normalized frequency (ω/ω_p) for $\kappa = 0$ (i.e., a lossless waveguide). As seen in Fig. 2(a), all modes have divergent wave vectors at a free-space energy of 1.73 eV (0.3 ω_p), corresponding to the surface plasmon resonance frequency (ω_{sp}) of Ag and TiO_2. Such divergent wave vectors are typical for lossless plasmonic systems. For a non-Hermiticity parameter $\kappa = 0$, $\epsilon(x) = \epsilon(-x)$, and all distinct modes have definite magnetic field parities with respect to x: modes B_1 and B_3 are odd with respect to $x = 0$ (the midpoint between the five-layer MIMIM waveguide), while modes B_2 and B_4 are even. Note that modes below ω_{sp} are positive index modes, while modes above ω_{sp} are negative index modes [17,47].

A simple way of rationalizing these four MIMIM modes is through the concept of coupled systems. The five-layer MIMIM waveguide is effectively a system of two coupled three-layer MIM waveguides as denoted in Fig. 1(b). For $t_d =$ 30 nm, each MIM waveguide supports only two plasmonic modes: an even parity mode below ω_{sp} and an odd parity mode above the surface plasmon resonance frequency. When these two waveguides are coupled together to form the five-layer waveguide of Fig. 1(a), even and odd superpositions of the two lowest order plasmonic modes form four distinct branches B_1–B_4. This feature can be clearly observed in panels (b)–(e) of Fig. 2, which plot the real part of $H_y(x)$ and z component of the mode Poynting vector (side panels) for each branch. For modes B_1 and B_2, the fields are indeed in- or out-of-phase superpositions of even MIM modes. In contrast, modes B_3 and B_4 are superpositions of odd MIM modes.

As the non-Hermiticity parameter κ is increased, the wave vectors begin to move into the complex plane. For example, Fig. 3(a) shows the dispersion curves of the MIMIM structure

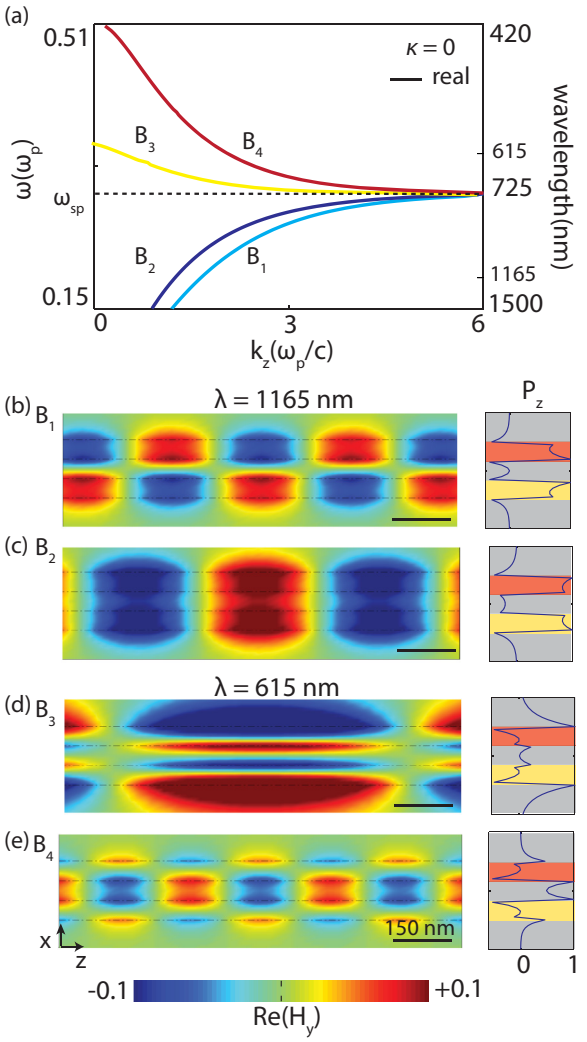

FIG. 2. (Color online) Dispersion curves (a) and spatial distribution of the real part of H_y for each branch B_1–B_4 (b)–(e) when $\kappa = 0$. The dashed line in panel (a) shows the surface plasmon resonance frequency ω_{sp}. The side panels of (b)–(e) show the distribution of the normalized Poynting vector along the stacking direction x. In field profile panels the black dashed lines show the boundaries of the layers.

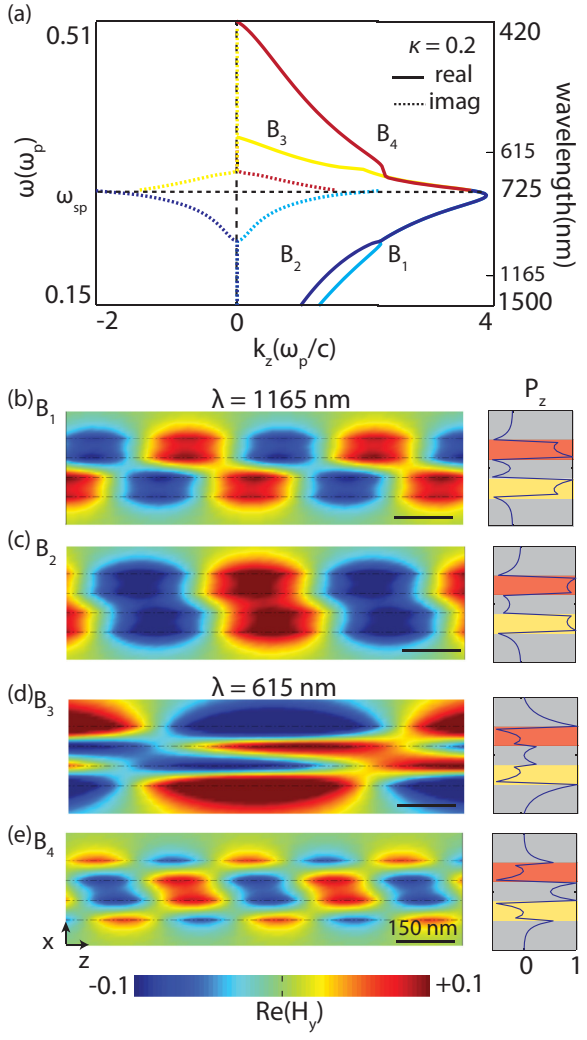

FIG. 3. (Color online) Dispersion curves (a) and spatial distribution of the real part of H_y for each branch B_1–B_4 (b)–(e) when $\kappa = 0.2$ at two wavelengths in the unbroken phase. The dashed line in panel (a) shows the surface plasmon resonance frequency ω_{sp}. The side panels of (b)–(e) show the distribution of the normalized Poynting vector along the stacking direction x.

for $\kappa = 0.2$ (the next section will highlight trends as a function of κ). Below the surface plasmon resonance, modes B_1 and B_2 appear to coalesce at an energy of 1.34 eV (0.23 ω_p), while above the surface resonance frequency, B_3 and B_4 merge at 1.8 eV (0.31 ω_p). Beyond these "exceptional points" (EP), the wave vectors become complex conjugate pairs. Therefore, they can be distinguished in the imaginary plane: One mode corresponds to an exponentially-growing mode along the propagation axis (z), while the other exhibits exponential decay. It should be noted that the propagation constant is complex beyond the exceptional point, even though the loss and gain values in the dielectric layers are always balanced.

The bottom panels of Fig. 3, (b)–(e), show the distribution of H_y for $\kappa = 0.2$. As in Fig. 2, field profiles are shown for wavelengths of 1165 and 615 nm, corresponding to energies less than and greater than the exceptional point energies, respectively. As seen, the distributions of the fields are not symmetric. Notably, the fields become skewed compared to their lossless counterparts, and, as discussed below, begin to appear more similar to each other as the exceptional point is approached. However as the side graph in each panel shows, the power is still distributed symmetrically with respect to x, which is consistent with having a real propagation constant in these regions. As the symmetry of the power is still preserved with respect to x, these regions are called "unbroken" phases of the PT system.

Figs. 4(a) and 4(b) shows the distribution of the real part of $H_y(x)$ at frequencies very close to, but still within, the unbroken phase regime. Here, it can be clearly observed that the distribution of B_1 approaches that of B_2 while that of B_3 evolves toward B_4. Similarly, while the modal energy is distributed symmetrically with respect to the x axis, it becomes quite similar for the two merged modes. These features indicate that the crossing of the branches is not a simple degeneracy

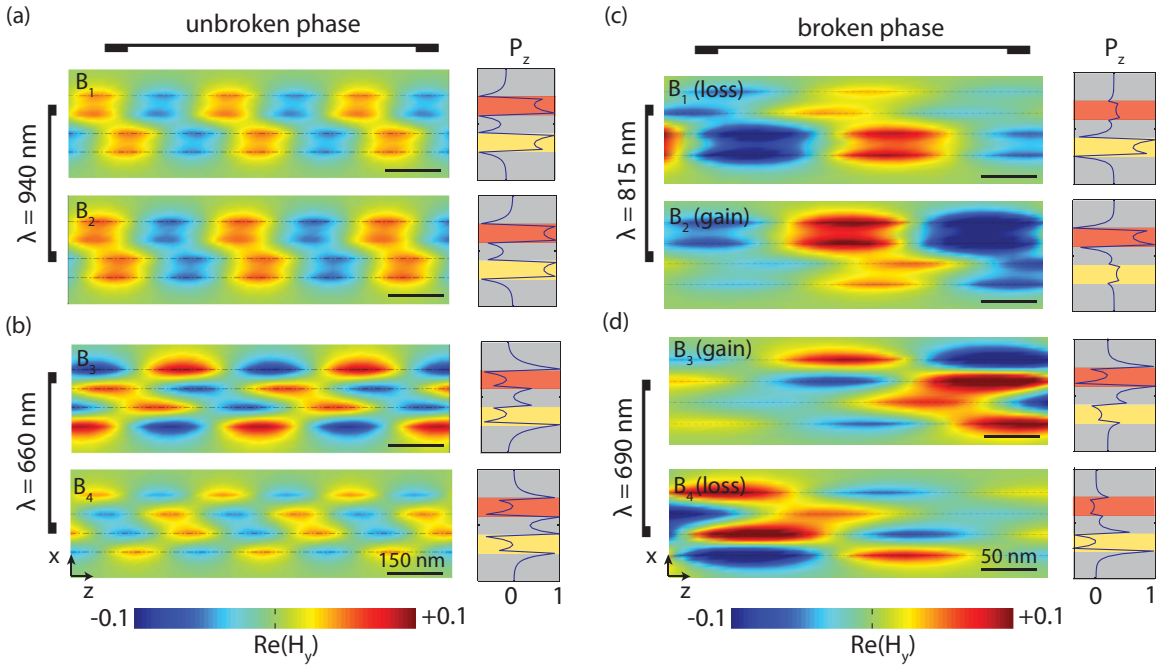

FIG. 4. (Color online) H_y field distribution of the four branches of the five-layer MIMIM, considering $\kappa = 0.2$. In panels (a) and (b), the energies are chosen close to the exceptional point, but still in the unbroken phase regime. In panels (c) and (d), field distributions are plotted in the broken phase regime. Each plot includes a cross section of the normalized Poynting vector at $z = 0$. Note that the scale bars are different in the left and right columns.

of states with multiplicity of 2 (i.e., having two different field profiles with the same energy), but instead a coalescence of two states.

In contrast, Figs. 4(c) and 4(d) illustrate the fields and power profiles for frequencies in the merged region of the dispersion curves. Here, the modes again become distinguishable, both in their complex wave vector and in their field localization. While they have the same phase velocity, they are either growing or decaying in amplitude as they propagate along the waveguide. Accordingly, the fields concentrate exclusively in either the gain region (modes B_2, B_3) or the loss region (modes B_1, B_4) of the waveguide. Further, this asymmetric field concentration is accompanied by an asymmetric power distribution: For the decaying/growing modes, power is concentrated in the loss/gain regions, respectively. Due to this asymmetry, this region is termed a "broken" phase of the system.

B. Waveguide coupling and its effect on exceptional point

In this section, we explore the effect of coupling between the gain and loss regions of the MIMIM waveguide, controlled via the metal thickness t_m. As will be shown, such coupling not only determines the exceptional point energy, but also which modes coalesce. We consider $t_m = 30$ nm, as in the prior section, and also $t_m = 50$ nm and 20 nm. As before, we keep the dielectric layer thicknesses fixed at $t_d = 30$ nm, to maintain the same number of waveguide modes. Figure 5 plots the exceptional point energy as a function of the non-Hermiticity parameter κ. For brevity, we only show the merging of mode B_1 in this figure. As seen, for fairly large thicknesses, $t_m = 30$ nm and 50 nm, this mode merges with B_2. By increasing κ or increasing the metal thickness (i.e., decreasing the coupling), the exceptional point shifts to lower energies. Though not shown, for modes above ω_{sp} (B_3, B_4), the exceptional point occurs at higher energies with increasing non-Hermiticity parameter and decreased waveguide coupling. For $t_m = 30$ nm and 50 nm, the waveguides are not strongly coupled, and coupled mode theory (CMT) can be used to describe the behavior [48]. CMT analysis (not shown) indicates that the exceptional point occurs where the coupling coefficient and the loss of the three-layer MIM modes are identical.

As the metal thickness is reduced to 20 nm, mode B_1 no longer merges with mode B_2 and instead merges with mode B_4. The merging of a positive and negative index mode is illustrated in the dispersion diagrams of Fig. 6. For a zero non-Hermiticity parameter, four distinct modes exist, similar to the dispersion for waveguides with $t_m = 30$ nm. As the

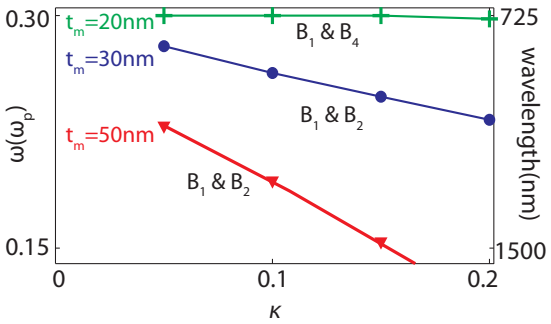

FIG. 5. (Color online) Exceptional point energy as a function of κ. The results are shown for the merging behavior of B_1, the mode below ω_{sp}, for $t_m = 20$, 30, and 50 nm. Note that t_m in the thickness of the intermediate metallic layer determining the coupling between two MIM waveguides.

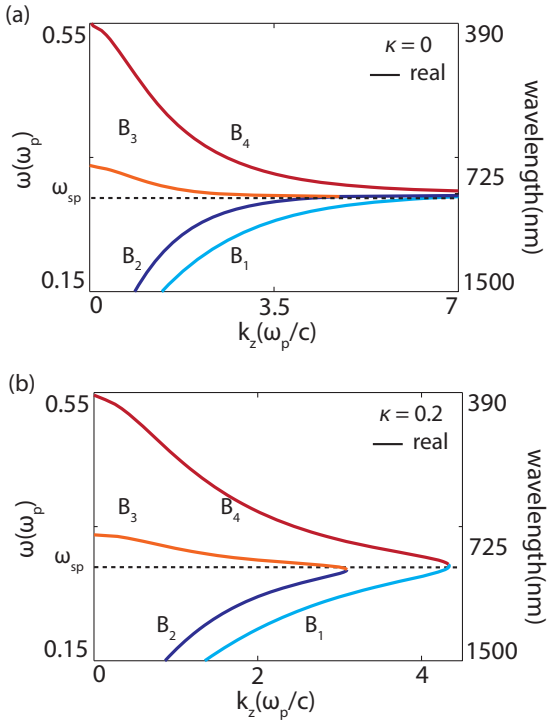

FIG. 6. (Color online) Real part of the dispersion curves of the five-layer MIMIM waveguide with $t_d = 30$ nm and $t_m = 20$ nm. The non-Hermiticity parameter is 0 and 0.2 in (a) and (b), respectively.

non-Hermiticity parameter is increased, modes B_1 and B_4 merge together while B_2 and B_3 merge. As seen in Figs. 5 and 6, this exceptional point energy is along the surface plasmon resonance frequency (ω_{sp}), and is approximately constant with increasing κ. We will later use a perturbational analysis to explain which modes merge in a multimodal system.

C. Nonplasmonic modes in PT-symmetric potentials

As a final specific example of PT-symmetric potentials in nanophotonic waveguides, we consider the behavior when the number of waveguide modes is increased by increasing the thickness of the dielectric core layers. Figure 7 plots the

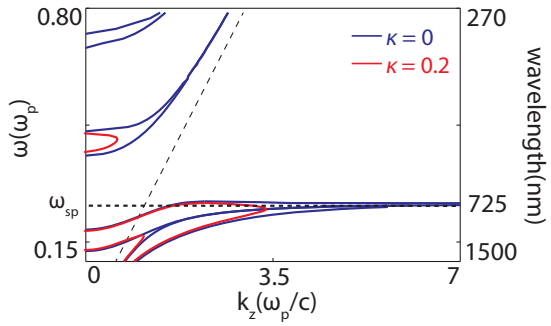

FIG. 7. (Color online) Dispersion curves of the five-layer MIMIM waveguide of Fig. 1(a) for $\kappa = 0$ (solid blue line) and 0.2 (solid red line). The thickness of the dielectric layers (t_d) and metallic layer (t_m) is 100 nm and 30 nm, respectively. The black dashed line shows the TiO_2 light line, and the dotted line corresponds to ω_{sp}.

dispersion curves for a five-layer MIMIM waveguide with metal thicknesses of 30 nm and dielectric thicknesses of 100 nm. Note that for clarity we only show modes with a purely real propagation constant. When $\kappa = 0$ (blue line), there are eight distinct branches: Two are similar to the plasmonic modes B_1 and B_2 already investigated, two are hybrid "plasmonic-photonic" modes, and four are photonic modes, which have wave vectors exclusively smaller than those in the dielectric (the light line is shown as a black dashed line in Fig. 7). When the non-Hermiticity parameter is increased to 0.2, the modes begin merging. As seen in the red curves of Fig. 7, the modes merge together based on their energy and propagation constant. The plasmonic modes merge with the hybrid plasmonic-photonic modes, while the purely photonic modes merge with each other. For the lower-energy photonic modes, real wave vectors exist only in a very narrow band. The higher-energy photonic modes with real propagation constants completely disappear for $\kappa = 0.2$. Note that the disappearance or quenching of the modes is a continuous phenomena, in that increasing κ causes more real branches to merge and disappear.

III. PERTURBATIONAL APPROACH TO NON-HERMITIAN NANOPHOTONICS

The above examples illustrated how modes merged when subjected to PT-symmetric potentials: Merging modes always had opposite parity and similar energies. In this section, we address whether these results are general to PT-symmetric optical systems (it turns out they are). To do so, we apply a perturbation analysis that gives key insight into the merging phenomena, describes the state coalescence, and describes this property based on the symmetries of the states.

A. Hamiltonian formulation and perturbation theory for wave propagation in multilayer waveguides

First, we begin by arranging Maxwell's equation in Hamiltonian format [49,50], to make them more suitable for a perturbational analysis. We focus on TM modes, though the results can be readily extended to more general hybrid modes. Assuming no spatial variation along y, the TM modes have only (E_x, E_z, H_y) nonzero field components and are described by

$$-i\frac{\partial}{\partial z}\hat{B}\begin{pmatrix}\hat{x}E_x(x,z)\\ \hat{y}H_y(x,z)\end{pmatrix} = \hat{H}\begin{pmatrix}\hat{x}E_x(x,z)\\ \hat{y}H_y(x,z)\end{pmatrix}. \tag{2}$$

Here,

$$\hat{B} = \begin{bmatrix}0 & -\hat{z}\times\\ \hat{z}\times & 0\end{bmatrix} \tag{3}$$

and

$$\hat{H} = \begin{bmatrix}\omega\epsilon_0\epsilon(x) & 0\\ 0 & \omega\mu_0 + \frac{1}{\omega\epsilon_0}\frac{\partial}{\partial x}\left(\frac{1}{\epsilon(x)}\frac{\partial}{\partial x}\right)\end{bmatrix}. \tag{4}$$

Defining

$$|\vec{F}\rangle = \begin{pmatrix}\hat{x}E_x(x,z)\\ \hat{y}H_y(x,z)\end{pmatrix} \tag{5}$$

one can rewrite Eq. (2) in Dirac notation as

$$-i\frac{\partial}{\partial z}\hat{B}\,|\vec{F}\rangle = \hat{H}\,|\vec{F}\rangle\,. \tag{6}$$

For waveguide modes of the system that vary as e^{izk_z}, the propagation constant of k_z and the spatial distribution are given by

$$k_z\hat{B}\,|\vec{F}(x)\rangle = \hat{H}\,|\vec{F}(x)\rangle\,. \tag{7}$$

If $|\vec{F}\rangle$ is a solution of Eq. (6), the expectation value of $\hat{B}$ will be determined as

$$\langle\hat{B}\rangle = \langle\vec{F}|\hat{B}|\vec{F}\rangle = 2\int_{-\infty}^{\infty} Re(E_x(x,z)H_y^*(x,z))dx = 4P_z(z). \tag{8}$$

Throughout the rest of this work we assume that the lossless modes are normalized in such a way that $\langle\hat{B}\rangle = 1$.

Likewise, the expectation values of $\langle\hat{H}\rangle$ will be given by

$$\begin{aligned}\langle\hat{H}\rangle = \langle\vec{F}|\hat{H}|\vec{F}\rangle &= \omega\epsilon_0\int_{-\infty}^{\infty}\epsilon(x)|E_x(x)|^2\,dx \\ &+ \omega\mu_0\int_{-\infty}^{\infty}|H_y(x)|^2\,dx \\ &- \omega\epsilon_0\int_{-\infty}^{\infty}\epsilon^*(x)|E_z(x)|^2\,dx.\end{aligned} \tag{9}$$

From Eqs. (8) and (9) it can be observed that while $\hat{B}$ is always Hermitian, $\hat{H}$ is Hermitian only for real $\epsilon(x)$, i.e., lossless materials. For a general Hamiltonian $\hat{H} = \hat{H}_R + i\hat{H}_I$ (nonmagnetic materials are still assumed), the following relation holds for the expectation value of $\hat{H}_I$:

$$\kappa\delta = \langle\hat{H}_I\rangle = \langle\vec{F}|\hat{H}_I|\vec{F}\rangle = \omega\epsilon_0\int_{-\infty}^{\infty}\epsilon_i(x)|\vec{E}(x)|^2\,dx. \tag{10}$$

Note that $|\vec{E}(x)|^2$ in the above equation is the magnitude of the electric field vector, accounting for both the transverse and longitudinal components.

Starting from the lossless case where $\hat{H} = \hat{H}_R$ is Hermitian, one can show that the propagating modes are orthogonal via $\hat{B}$, i.e., $\langle\vec{F}_{k_z'}|\hat{B}|\vec{F}_{k_z}\rangle = \delta_{k_zk_z'}$. Further, for the specific arrangement of Fig. 1(a), $\hat{H}_R$ is even with respect to x, so that the modes have definite even or odd parities with respect to x. However, when κ is increased, the Hamiltonian ceases to be Hermitian. For small values of the non-Hermiticity parameter, one can treat $i\hat{H}_I$ as a perturbation to the system. Utilizing the Rayleigh-Schrodinger perturbation method [51], and considering the orthogonality of 0th order modes via $\hat{B}$, the following equations can be derived for 1st and 2nd order corrections to the propagation constants of the lossless waveguide:

$$k_{zn}^{(1)} = i\left\langle\vec{F}_n^{(0)}\middle|\hat{H}_I\middle|\vec{F}_n^{(0)}\right\rangle \tag{11a}$$

$$k_{zn}^{(2)} = -\sum_{m,m\neq n}\frac{\left|\left\langle\vec{F}_n^{(0)}\middle|\hat{H}_I\middle|\vec{F}_m^{(0)}\right\rangle\right|^2}{k_{zn}^{(0)} - k_{zm}^{(0)}}. \tag{11b}$$

Considering that $\hat{H}_R$ is an even function with respect to x while $\hat{H}_I$ is odd, and considering that the modes of the lossless waveguide (0th order modes) have definite parities, it can be seen that $k_{zn}^{(1)}$ vanishes for all states. In other words the 1st order correction for the modes of the lossless waveguide is identically zero for all states.

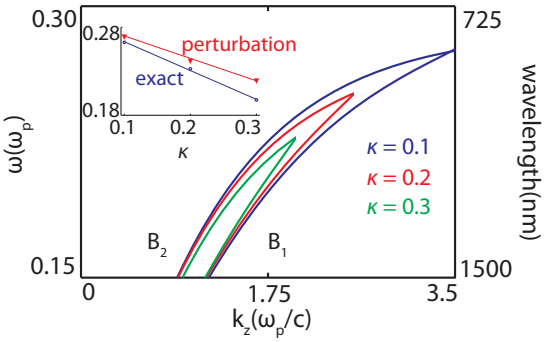

FIG. 8. (Color online) Second order perturbational correction of propagation constants for modes B_1 and B_2 of the MIMIM waveguide when κ equals 0.1, 0.2, and 0.3. Here, the metal and dielectric thicknesses are $t_m = t_d = 30$ nm. The inset shows the comparison between the energies of the exceptional points calculated via the perturbational method and the exact approach.

In contrast, the 2nd correction of $k_{zn}^{(2)}$ is not zero, and its value depends on the overlap integral:

$$\left\langle\vec{F}_n^{(0)}\middle|\hat{H}_I\middle|\vec{F}_m^{(0)}\right\rangle = \omega\epsilon_0\int_{-\infty}^{\infty}\epsilon_i(x)\vec{E}_n^{(0)*}(x).\vec{E}_m^{(0)}(x)dx. \tag{12}$$

Notably, Eq. (12) has nonzero values only for modes of opposite parities, consistent with all of our case studies in the prior section.

The presence of the minus sign in front of Eq. (11b) arises from the anti-Hermiticity of the perturbing operator and has a significant physical meaning. Here, unlike a Hermitian perturbation which leads to an energy splitting hence state repulsion, the fundamental mode is raised while the 1st exited state is lowered and the separation of the propagation constants decreases. This result means that unlike Hermitian perturbations, here the perturbed eigenvalues approach each other. We will elaborate more on this concept in the next section.

Figure 8 shows the dispersion of modes B_1 and B_2 calculated through Eq. (11b) for $\kappa = 0.1$, 0.2, and 0.3. As in Eq. (12), the larger the non-Hermiticity parameter κ, the stronger the perturbation—meaning that modes merge at lower energies. This behavior can be clearly observed in Fig. 5 where the crossing point occurs at lower energies for larger κ. Note that the real wave vectors and exceptional points show very good agreement between both our exact analytic and perturbational approaches, as illustrated in the inset of Fig. 8. Not surprisingly, the agreement between models begins to deviate with increasing κ, where higher order corrections are needed to accurately model the perturbed system. The appendix presents calculated results including higher order corrections, demonstrating improved accuracy.

B. State coalescence and generalized power

As a final application of our Hamiltonian formulation, we describe state coalescence and power flow along the waveguide. As described before, $\hat{H}$ is Hermitian at $\kappa = 0$,

so the modes of the lossless waveguide form an orthogonal, complete basis which can be used to find the equivalent matrix representation of any general Hamiltonian in Eq. (7). If $|\vec{F}_n^{(0)}\rangle$ represents the nth eigenvector of the Hermitian case ($\kappa = 0$) the matrix elements of $\hat{H}$ in this basis are given by $H_{nm} = \langle \vec{F}_n^{(0)}|\hat{H}|\vec{F}_m^{(0)}\rangle$. Here, we consider only two eigenvectors of the lossless waveguide (i.e., the ones that will merge together). However, it should be noted that the below formalism is still applicable if more modes are considered.

The general Hamiltonian $\hat{H}$ of a PT system in the basis of $\hat{H}_R$ can be written as

$$\hat{H} = \hat{H}_R + i\kappa\hat{H}_I = \begin{bmatrix} k_{z1} & 0 \\ 0 & k_{z2} \end{bmatrix} + i\kappa \begin{bmatrix} 0 & \delta \\ \delta^* & 0 \end{bmatrix}, \tag{13}$$

where k_{z1} and k_{z2} are the propagation constants of the lossless waveguide, κ is the non-Hermiticity parameter, and δ is the overlap integral given by Eq. (12). Note that the diagonal elements of the second matrix in Eq. (13) vanishes, resulting from the symmetry of the lossless modes described before. Also, due to the orthogonality of the lossless modes, $\hat{B}$ is an identity matrix. So according to Eq. (7), the eigenvalues of the matrix in Eq. (13) are indeed the propagation constants of the modes in a PT-symmetric waveguide with non-Hermiticity parameter κ. The eigenvalues are given by

$$k_{z\pm} = \frac{(k_{z2} + k_{z1}) \pm \sqrt{(k_{z2} - k_{z1})^2 - 4\kappa^2|\delta|^2}}{2}. \tag{14}$$

For a small non-Hermiticity parameter, where $2\kappa|\delta| \ll (k_{z2} - k_{z1})$, the above equation is simplified to Eq. (11b), directly obtained from perturbation theory. However, this equation is more general and valid even for large values of κ. From Eq. (14), one can observe that the two roots become the same when $|k_{z2} - k_{z1}| = 2\kappa|\delta|$, hence the formation of an exceptional point. This equation analytically determines the amount of non-Hermiticity parameter κ the system can tolerate without entering into the broken phase beyond the exceptional point. Right at the exceptional point, the propagation constant is in fact the average of the propagation constants of the lossless waveguide, $\frac{k_{z2}+k_{z1}}{2}$.

Solving for the eigenvectors of Eq. (13), we find the modes of the PT-symmetric waveguide as well. The eigenvectors are

$$\begin{bmatrix} a_1 \\ a_2 \end{bmatrix}_\pm = \begin{bmatrix} 1 \\ i\frac{(k_{z1}-k_{z2}) \mp \sqrt{(k_{z2}-k_{z1})^2 - 4\kappa^2|\delta|^2}}{2\kappa\delta} \end{bmatrix}. \tag{15}$$

At the EP, the states superimpose with a $\pi/2$ phase difference and the same weight, i.e., $|a_{2\pm}| = 1$. Also note that when the eigenvalues become identical, there is only one eigenstate, verifying the mode coalescence. Before the exceptional point, two real, distinguishable propagation constants are given by Eq. (14). In this regime, the system supports two different but nonorthogonal modal solutions, based on Eq. (15):

$$\begin{aligned} |\vec{F}\rangle_+ &= e^{izk_{z+}}\left(|\vec{F}_1^{(0)}\rangle + a_{2+}|\vec{F}_2^{(0)}\rangle\right) \\ |\vec{F}\rangle_- &= e^{izk_{z-}}\left(|\vec{F}_1^{(0)}\rangle + a_{2-}|\vec{F}_2^{(0)}\rangle\right). \end{aligned} \tag{16}$$

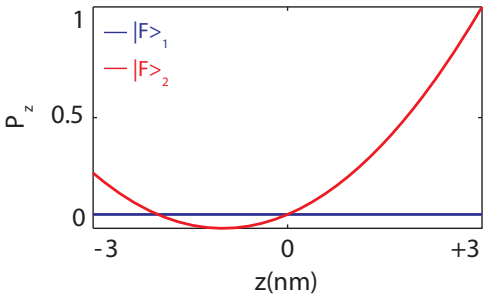

FIG. 9. (Color online) Power propagation at $x = 0$ for the MIMIM waveguide at the exceptional point for $k = 0.1$. The values are normalized to show the relative power of each mode.

At and beyond the EP, the two above solutions become

$$|\vec{F}\rangle_1 = e^{iz\frac{k_{z1}+k_{z2}}{2}}\left(|\vec{F}_1^{(0)}\rangle - i|\vec{F}_2^{(0)}\rangle\right) \tag{17}$$

and

$$|\vec{F}\rangle_2 = e^{iz\frac{k_{z1}+k_{z2}}{2}}\left((1+z)|\vec{F}_1^{(0)}\rangle - i\left(1 + z - \frac{i}{k\delta}\right)|\vec{F}_2^{(0)}\rangle\right). \tag{18}$$

Assuming $\langle\hat{B}\rangle$ is normalized, then the power of the second state is given by $2(1+z)^2 + \frac{1}{\kappa^2|\delta|^2}$. Figure 9 shows the dependency of the power of these two solutions along the z direction. As seen, while $|\vec{F}\rangle_1$ has a constant power along the waveguide, the power of $|\vec{F}\rangle_2$ varies quadratically with z. The presence of the z dependency in the power flow in this case is a signature of the EP in the system. Here the difference between the degeneracy and the EP is clear. While in the degenerate case one has an eigenvalue and various modal type eigenvectors, at and above the EP, only one mode exists. The second solution is not a mode in the typical sense, since (as aside from the exponential factor), its shape is also z dependent.

Accordingly, there are three distinct regimes that describe modes in a PT-symmetric system. Below the exceptional point, the system is in the unbroken phase, there are distinguishable propagating modes, and the power remains constant upon propagation. Right at the exceptional point, the system supports two very different solutions. While one mode is propagating and preserves power upon propagation, the other solution has a quadratic power dependency in the direction of propagation. In the broken regime, above the exceptional point, the propagation constants depart from purely real values and appear as complex conjugate pairs. There, one can find an exponential growth or decay of the modal power upon propagation.

As evidenced above, power is not conserved in a PT-symmetric potential. It only is conserved when the system is in an unbroken phase where the field profiles have definite parities, $|E|^2$ is even, and the power distributes itself symmetrically in the system. There, due to the odd parity of $\epsilon_I(x)$, $\langle\hat{H}_I\rangle$ vanishes and power does not vary as it propagates along the waveguide. However, in a PT system, we can define a generalized

power as

$$Q(z) = \langle \vec{F}(-x,z)|\hat{B}|\vec{F}(x,z)\rangle\,. \tag{19}$$

A brief check shows that this quantity has the dimension of power. Also note that if the system is Hermitian (i.e., $\kappa = 0$) or if it is PT symmetric but in the unbroken phase, Q is simplified to the typical definition of power. The evolution of Q is given by the following equation as

$$\begin{aligned}\frac{dQ}{dz} &= \left\langle \hat{B}\frac{\partial \vec{F}(-x,z)}{\partial z}|\vec{F}(x,z)\right\rangle + \left\langle \vec{F}(-x,z)|\hat{B}\frac{\partial \vec{F}(x,z)}{\partial z}\right\rangle \\ &= \langle i\hat{H}(-x)\vec{F}(-x,z)|\vec{F}(x,z)\rangle + \langle \vec{F}(-x,z)|i\hat{H}(x)\vec{F}(x,z)\rangle \\ &= i\,\langle \vec{F}(-x,z)|\hat{H}(x) - \hat{H}^{\dagger}(-x)|\vec{F}(x,z)\rangle \Rightarrow \frac{dQ}{dz} = 0.\end{aligned} \tag{20}$$

This result implies that generalized power is always conserved in a PT-symmetric system, whether the system is in the unbroken phase, right at the exceptional point, or in the broken phase.

IV. CONCLUSION

In conclusion, we have studied the behavior of a PT-symmetric plasmonic waveguide, where the PT potential arises from loss/gain balance in the dielectric permittivity. Through an exact modal solution, we derived the propagation constants and field distributions of the four lowest order modes of the waveguide. We investigated the modal behavior as a function of a non-Hermiticity parameter, giving particular attention to state coalesce and evolution of the exceptional points. We also showed that waveguide-layer coupling can control PT modal properties and coalescence. The results were rationalized through a Hamiltonian formulation of the waveguide, which allowed development of a perturbational analysis and insight into state coalescence before, after, and right at the exceptional point.

These results may enable the design of PT-symmetric plasmonic devices, including nanophotonic modulators with gain. In particular, systems near the exceptional point will exhibit very rapid and significant modal transformations, giving rise to fast, sensitive, and low-power all-optical modulators. These results could also be extended to investigate nonlinear PT-symmetric waveguides, with the aim of making asymmetric and nonreciprocal nanophotonic devices. More generally, PT-symmetric plasmonics may enable a class of nanophotonic devices—from optical diodes to nonrecripocal reflectors—based on a judicious balance of loss and gain media.

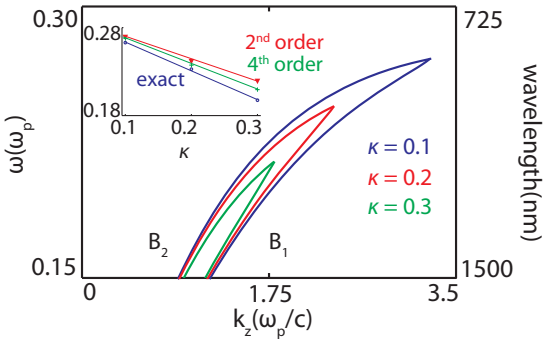

FIG. 10. (Color online) Fourth order perturbational correction of propagation constants for modes B_1 and B_2 of the MIMIM waveguide when κ equals 0.1, 0.2, and 0.3. Here, the metal and dielectric thicknesses are $t_m = t_d = 30$ nm. The inset shows the comparison between the energies of the exceptional points calculated via the perturbational method (2nd and 4th) and the exact results.

ACKNOWLEDGMENTS

The authors acknowledge the entire Dionne group for very insightful feedback on the manuscript. This work is supported in part by a SLAC National Accelerator Laboratory LDRD award in concert with the Department of Energy, Office of Basic Energy Sciences, Division of Materials Sciences and Engineering, under contract DE-AC02-76SF00515. Funding from the Hellman Faculty Scholars program and a National Science Foundation CAREER Award (DMR-1151231) are also gratefully acknowledged.

APPENDIX: PERTURBATIONAL ANALYSIS INCLUDING HIGHER ORDER CORRECTIONS

As mentioned in the text, the perturbational analysis can include higher orders of correction to increase the accuracy of the approximation. Here, we extend the method up to the next nonzero order correction, i.e., fourth order. The correction to the propagation constant is given by

$$k_{zn}^{(4)} = -\sum_{i,m,i,m\neq n} \frac{\left|\langle \vec{F}_n^{(0)}|\hat{H}_I|\vec{F}_i^{(0)}\rangle\right|^2 \left|\langle \vec{F}_n^{(0)}|\hat{H}_I|\vec{F}_m^{(0)}\rangle\right|^2}{\left(k_{zn}^{(0)} - k_{zm}^{(0)}\right)\left(k_{zn}^{(0)} - k_{zi}^{(0)}\right)^2} + \sum_{i,m,k,i,m,k\neq n} \frac{\langle \vec{F}_i^{(0)}|\hat{H}_I|\vec{F}_m^{(0)}\rangle\langle \vec{F}_m^{(0)}|\hat{H}_I|\vec{F}_k^{(0)}\rangle\langle \vec{F}_k^{(0)}|\hat{H}_I|\vec{F}_n^{(0)}\rangle\langle \vec{F}_n^{(0)}|\hat{H}_I|\vec{F}_i^{(0)}\rangle}{\left(k_{zn}^{(0)} - k_{zi}^{(0)}\right)\left(k_{zn}^{(0)} - k_{zm}^{(0)}\right)\left(k_{zn}^{(0)} - k_{zk}^{(0)}\right)}. \tag{A1}$$

Figure 10 shows the calculated propagation constant when including this higher order correction. The figure inset clearly indicates improved accuracy compared to the 2nd order correction. However, note that caution is advised when including even higher order corrections. Due to the recursive nature of this perturbational method, increased error might be observed after higher order corrections.

[1] J. Bravo-Abad and F. J. Garca-Vidal, Nat. Nanotechnol. **8**, 479 (2013).
[2] W. Zhou, M. Dridi, J. Y. Suh, C. H. Kim, D. T. Co, M. R. Wasielewski, G. C. Schatz, and T. W. Odom, Nat. Nanotechnol. **8**, 506 (2013).
[3] Z. L. Deng and J. W. Dong, Opt. Express **21**, 20291 (2013).
[4] K. Ding, M. T. Hill, Z. C. Liu, L. J. Yin, P. J. van Veldhoven, and C. Z. Ning, Opt. Express **21**, 4728 (2013).
[5] M. Khajavikhan, A. Simic, M. Katz, J. H. Lee, B. Slutsky, A. Mizrahi, V. Lomakin, and Y. Fainman, Nature (London) **482**, 204 (2012).
[6] K. Okamato, I. Niki, A. Shvartser, Y. Narukawa, T. Mukai, and A. Scherer, Nat. Mater. **3**, 601 (2004).
[7] C. W. Lai, J. An, and H. C. Ong, Appl. Phys. Lett. **86**, 251105 (2005).
[8] R. F. Oulton, V. J. Sorger, T. Zentgraf, R. M. Ma, C. Gladden, L. Dai, G. Bartal, and X. Zhang, Nature (London) **461**, 629 (2009).
[9] M. A. Noginov, G. Zhu, A. M. Belgrave, R. Bakker, V. M. Shalaev, E. E. Narimanov, S. Stout, E. Herz, T. Suteewong, and U. Wiesner, Nature (London) **460** 1110 (2009).
[10] W. Cai, J. S. White, and M. L. Brongersma, Nano Lett. **9**, 4403 (2009).
[11] J. A. Dionne, K. Diest, L. A. Sweatlock, and H. A. Atwater, Nano Lett. **9**, 897 (2009).
[12] V. E. Babicheva, N. Kinsey, G. V. Naik, M. Ferrera, A. V. Lavrinenko, V. M. Shalaev, and A. Boltasseva, Opt. Express **21**, 27326 (2013).
[13] L. A. Sweatlock and K. Diest, Opt. Express **20**, 8700 (2012).
[14] A. Raman and S. Fan, Phys. Rev. B **83**, 205131 (2011).
[15] L. Liu, Z. Han, and S. He, Opt. Express **13**, 6645 (2005).
[16] J. A. Dionne, L. A. Sweatlock, H. A. Atwater, and A. Polman, Phys. Rev. B **72**, 075405 (2005).
[17] J. A. Dionne, E. Verhagen, A. Polman, and H. A. Atwater, Opt. Express **16**, 19001 (2008).
[18] J. B. Lassiter, F. McGuire, J. J. Mock, C. Cirac, R. T. Hill, B. J. Wiley, A. Chilkoti, and D. R. Smith, Nano Lett. **13**, 5866 (2013).
[19] R. F. Oulton, V. J. Sorger, D. A. Genov, D. F. P. Pile1, and X. Zhang1, Nat. Photonics **2**, 496 (2008).
[20] S. Pandey, B. Gupta, and A. Nahata, Opt. Express **21**, 24422 (2013).
[21] A. V. Krasavin and A. V. Zayats, Opt. Express **18**, 11791 (2010).
[22] V. J. Sorge, N. D. Lanzillotti-Kimura, R.-M. Ma, and X. Zhang, Nanophotonics **1**, 17 (2012).
[23] A. V. Krasavin and A. V. Zayats, Phys. Rev. Lett. **109**, 053901 (2012).
[24] A. Christofi and N. Stefanou, Phys. Rev. B **87**, 115125 (2013).
[25] K. Fang, Z. Yu, V. Liu, and S. Fan, Opt. Lett. **36**, 4254 (2011).
[26] Z. Wang and S. Fan, Opt. Lett. **30**, 1989 (2005).
[27] Z. Yu, Z. Wang, and S. Fan, Appl. Phys. Lett. **90**, 121133 (2007).
[28] C. M. Bender and S. Boettcher, Phys. Rev. Lett. **80**, 5243 (1998).
[29] C. M. Bender, S. Boettcher, and P. N. Meisinger, J. Math. Phys. **40**, 2201 (1999).
[30] C. M. Bender, M. V. Berry, and A. Mandilara, J. Phys. A: Math. Gen. **35**, L467 (2002).
[31] G. A. Mezincescu, J. Phys. A: Math. Gen **33**, 4911 (2000).
[32] Z. Lin, H. Ramezani, T. Eichelkraut, T. Kottos, H. Cao, and D. N. Christodoulides, Phys. Rev. Lett. **106**, 213901 (2011).
[33] L. Feng, M. Ayache, J. Huang, Y.-L. Xu, M.-H. Lu, Y.-F. Chen, Y. Fainman, and A. Scherer, Science **333**, 729 (2011).
[34] L. Feng, Y.-L. Xu, W. S. Fegadolli, M.-H. Lu, J. E. B. Oliveira, V. R. Almeida, Y.-F. Chen, and A. Scherer, Nat. Mater **12**, 108 (2013).
[35] S. Klaiman, U. Günther, and N. Moiseyev, Phys. Rev. Lett. **101**, 080402 (2008).
[36] S. Longhi, Phys. Rev. A **82**, 031801(R) (2010).
[37] A. E. Miroshnichenko, B. A. Malomed, and Y. S. Kivshar, Phys. Rev. A **84**, 012123 (2011).
[38] Y. D. Chong, L. Ge, and A. D. Stone, Phys. Rev. Lett. **106**, 093902 (2011).
[39] M.-A. Miri, A. Regensburger, U. Peschel, and D. N. Christodoulides, Phys. Rev. A **86**, 023807 (2012).
[40] M.-A. Miri, A. B. Aceves, T. Kottos, V. Kovanis, and D. N. Christodoulides, Phys. Rev. A **86**, 033801 (2012).
[41] C. Li, C. Huang, H. Liu, and L. Dong, Opt. Lett. **37**, 4543 (2012).
[42] Z. H. Musslimani, K. G. Makris, R. El-Ganainy, and D. N. Christodoulides, Phys. Rev. Lett. **100**, 030402 (2008).
[43] Y. He, X. Zhu, D. Mihalache, J. Liu, and Z. Chen, Phys. Rev. A **85**, 013831 (2012).
[44] J. D'Ambroise, P. G. Kevrekidis, and S. Lepri, J. Phys. A: Math. Theor. **45**, 444012 (2012).
[45] P. B. Johnson and R. W. Christy, Phys. Rev. B **6**, 4370 (1972).
[46] H. Alaeian and J. A. Dionne (2013), arXiv:1306.0059 [Phys. Rev. A (to be published)].
[47] E. Verhagen, R. de Waele, L. Kuipers, and A. Polman, Phys. Rev. Lett. **105**, 223901 (2010).
[48] A. Hardy and W. Streifer, J. Lightwave Technol. **3**, 1135 (1985).
[49] G. Zhu, J. Lightwave Technol. **29**, 905 (2011).
[50] M. Skorobogatiy, *Nanostructured and Subwavelength Waveguides: Fundamentals and Applications* (John Wiley and Sons, Chichester, UK, 2012).
[51] D. A. B. Miller, *Quantum Mechanics for Scientists and Engineers* (Cambridge University Press, New York, USA, 2008).